Direct Entorhinal Control of CA1 Temporal Coding

Matteo Guardamagna[1†], Oscar Chadney[1†], Federico Stella[2†], Qiangwei Zhang[1], Clifford Kentros[1,3,4], Francesco P. Battaglia[2,4*]

[1]Kavli Institute for Systems Neuroscience and Centre for Neural Computation, Norwegian University of Science and Technology, Trondheim, Norway.
[2]Donders Institute for Brain, Cognition and Behaviour, Radboud University, Nijmegen, the Netherlands.
[3]Institute of Neuroscience, University of Oregon, 1254 University of Oregon, Eugene, OR 97403, USA.
[4]Co-Senior Author.

*Corresponding author(s). E-mail(s): francesco.battaglia@donders.ru.nl;
Contributing authors: matteo.guardamagna@ntnu.no; oscar.m.t.chadney@ntnu.no; federico.stella@donders.ru.nl; qiangwei.zhang@ntnu.no; clifford.kentros@ntnu.no;
†These authors contributed equally to this work.

Abstract

Local computations of CA1 neurons are shaped by two direct input streams, from CA3 and EC LIII. By specifically silencing the direct input from the entorhinal cortex, we found that single-cell temporal coding (phase precession) strictly depends on direct EC-CA1 communication, while spatial coding and network oscillations are largely unaffected by the manipulation. Conversely, transient inhibition of the EC-CA1 direct pathway actually improved the temporal coordination of CA1 ensembles (theta sequences), reducing coding heterogeneity.

Main

Temporal coding at multiple scales, from milliseconds to seconds, is used by the brain to convey information and process parallel computations. Within the hippocampus, "theta sequences" [10, 11] of spikes from cells with consecutive place fields, rapidly sweeping through a theta oscillation cycle (≈100ms), are a prominent expression of temporal coding. Theta sequences have been linked to memory of events taking place at different times, prediction of future occurrences, and action planning, functions that require the comparison of previously stored traces with the current stream of information about the external world [5]. The hippocampal sub-field CA1 is an interesting candidate for this operation as it sits at the confluence of two inputs: an intra-hippocampal one through the CA3 sub-field [28] and an extra-hippocampal one from the Entorhinal Cortex Layer III (EC LIII; [28]), which are thought to carry, respectively, memorized and novel information [9, 6]. Classic theoretical models see phase precession, the correlation between the animal position and the firing phase of place cells within the theta cycle [20], as the generating mechanism of theta sequences [24, 25]. This does not take into account the influence of dual input to CA1, which may act by itself as a considerable source of variability. It also neglects multiple results indicating how phase precession and sequences, rather than being associated, tend to appear most strongly under different network states, which have been associated to prevalence of the EC LIII or CA3 inputs respectively [2, 30, 15]. While dynamical interactions between these inputs have been studied in detail [9, 2, 30, 15], including via the use of activity perturbations [4, 22, 31], dissecting their relative role is made difficult by the fact that EC LII also innervates CA3. Thus, standard, unspecific manipulations of EC end up affecting both input streams. Here, we address this issue with a combination of ensemble physiology, layer-resolved oscillation recording and highly-specific manipulation of EC LIII projections.

We used the enhancer-driven gene expression (EDGE) [3] to create a novel transgenic mouse cross expressing an inhibitory opsin, JAWS [8], restricted to EC LIII pyramidal cells (Figure 1a-h), whose projections directly reach the distal dendrites of CA1 pyramidal cells [28]). We quantified expression levels by counting the number of JAWS-GFP RNA-positive nuclei within all brain areas and we estimated that the majority (78 %) were in EC LIII (Figure 1c). The expression of JAWS-GFP was also largely overlapping with Purkinje cell protein 4 (PCP4)-positive neurons (Figure 1d-h and Figure S1a-d), which can be used as a marker for EC LIII neurons. We recorded both large CA1 pyramidal cell populations and layer resolved oscillations with a novel version of a Hybrid Drive, combining 13 independently movable tetrodes, one linear silicon probe and one optic fiber in a single device ([14, 15], Figure 1i). The optic fiber was positioned above (approx. 100 μm) the pyramidal layer and enabled optical manipulation of the direct EC LIII projection in s.l.m. (Figure 1j). Individual tetrodes spanned the CA1 proximo-distal axis, with the majority recording individual neurons from the intermediate CA1 region (Figure 1k,l). Animals were trained, in a familiar environment, to run back and forth on a linear track collecting food rewards at both ends. The light of the laser was delivered continuously (max 30 s, 20 mW at fiber tip) every other lap, for both running directions consecutively (Figure 1m and Figure S2).

We first examined the effect of EC LIII distal input suppression on the rate code of CA1 neurons (Figure 2a). Among pyramidal neurons we only selected those with significant spatial modulation (n=380 cells; see Place Cell Identification). Place fields were then divided into two groups: "locking" (n=142 cells) and "precessing" (n=238 cells), on the basis of their relationship with theta oscillations (as previously described in [15]) during Laser OFF periods. We found that both average and peak firing rate decreased during EC LIII transient deafferentation (Figure 2b,c; Kolmogorov–Smirnov test, $p<0.001$). Similarly, the size of the place field decreased following inhibition of EC LIII input (Figure 2d; Kolmogorov–Smirnov test, $p<0.001$). The manipulation similarly affected rate and place field response of both cell sub-populations. Effects were independent of changes in the running speed of the animals (Figure S3). Additionally, the observed effects did not derive from an intrinsic instability of the place field representations. When comparing odd and even laps within a single condition, no significant differences were found for the previously described rate and place field properties (Figure S4; Kolmogorov–Smirnov test., $p>0.05$ and Figure S6). Next, we explored in more detail the effects of the manipulation on place field dynamics. We computed the shift between conditions (Laser OFF vs. Laser ON) for the position of the place field start, center and end (Figure 2e-f). On average we found that both the place field start and end positions shrank toward the center of the place field (defined as the peak firing rate) during inhibition of EC LIII axons (Figure 2f). Both forward and backward shifts were statistically different from within-conditions controls (Kolmogorov–Smirnov one-sided test; mean shift start =+4.72 cm, $p=0.02$; mean shift end =-4.80 cm, $p=0.006$; Figure S5). Additionally, the shift of the place field end was larger for cells with higher theta score (Figure 2g), suggesting a specific loss of spiking activity in the second half of the field for cells with steeper precession. Similarly, the difference in mean firing rate between conditions was significantly modulated by the theta score, with a larger difference for cells with higher theta score (or phase precessing cells; Spearman's rho = 0.17, p-value = 0.0006, Figure 2h). Conversely, we found no modulation of the peak rate difference by the theta score (Spearman's rho = 0.07, p-value = 0.133 Figure 2i).

These results point to the fact that the EC LIII direct input is not essential for the consistent expression of a place field representation of a familiar environment (Figure 2j), as CA1 maps are stable across trials even in its absence (Figure S6).

We then asked how the transient inhibition of EC LIII input affects fine-scale temporal coding processes within the CA1 network. We found that the effects of the inhibition are mostly observable during periods of spontaneously elevated medium gamma (MG) power, consistent with the proposed link between MG and entorhinal influences on CA1 [9]. It has been previously shown [2, 15] that theta phase precession is strongest during elevated MG periods, in a subgroup of hippocampal place fields. Here we show that, EC LIII inhibition markedly reduce or eliminates phase precession, abolishing any difference between epochs dominated by MG or Slow gamma (SG) oscillations. The spike density plots in Figure 3a (top row) reveal how spikes of phase precessing cells in the early phases of the theta cycle are reduced during periods of EC LIII inhibition, diluting phase precession (Figure 3a, bottom row; Kolmogorov-Smirnov on spike densities, $p<0.001$). The contour regions of highest spike density

further reveal how the population of phase precessing cells is more affected by the optogenetic manipulation, while the pattern of phase locking cells is left largely intact. This effect is still visible when the analysis is performed on a cell-by-cell basis. Under normal conditions, with increasing dominance of medium gamma, phase precessing cells show a steeper phase-position slope (Figure 3b, left panel; replication of [15]). However, during periods of EC LIII inhibition, such correlation is removed. Together, these observations show how the EC LIII afferent control is crucial for the normal expression of theta phase precession in CA1.

Since its discovery, phase precession, and the resulting temporal distribution of place field spikes, has been named as the "engine" underlying the formation of theta sequences [24]. We have previously called this hypothesis into question by showing at least a partial dissociation between the expression of precession and sequences. Here, we therefore asked how the generation of neuronal sequences in CA1 is affected by EC LIII afferent inhibition. We first addressed this question by quantifying the correlation between field spacing and average theta phase separation of place cell pairs, an index of how consistently neurons fire in a stable sequence [24, 10].

The spatio-temporal correlation improved during periods of EC LIII inhibition (Laser ON; Figure 3c), regardless of whether slow gamma and medium gamma dominated the LFP (Kolmogorov–Smirnov test, $p<0.01$). Elevated slow gamma-network states retained the highest spatio-temporal ordering in both conditions. Precessing and locking cells form two groups of neurons that express theta sequences in a largely decoupled fashion [15]. Here, we asked how inhibiting EC LIII inputs affects the association between these two cell groups. In fact, overall correlations increased during EC LIII inhibition, with cells from both groups expressing the highest ordering during slow gamma states (Figure 3d). Phase precessing cells improved their spatio-temporal correlations among themselves and with phase locking cells (i.e. with both phase precessing and phase locking cells; Figure 3d, left panel), while phase locking cells only improved their correlations with cells of the other group (i.e., with phase precessing cells; Figure 3d, right panel). Notably, when EC LIII inhibition is applied, within and across group correlations became indistinguishable. Thus, by releasing a subset of place fields from the influence of the EC LIII input, CA1 neurons express sequences in a coherent way across the population, eliminating the differentiation between groups observed under normal input conditions. We confirmed and expanded these results by applying a Bayesian decoder (Figure 3e), looking at coding of current animal position and sequence expression across CA1 neuron populations (Figure 3f). We found an enhancement of sequential coding during periods of inhibition of EC LIII input (right panel; Paired t-test, $p=0.0074796$). Additionally, the sequential decoding improved in the second half of the theta cycle (across all conditions and network states; Figure S7a-b right panels) while positional decoding remained largely unchanged (Figure 3e left panel and Figure S7a-b left panels).

Last, we explored the effects of the manipulation on global oscillatory rhythms. We applied Current Source Density analysis (CSD), to extract layer-specific theta (6-10 Hz) and gamma oscillations (20-90 Hz). We found no alterations in the theta power profile (6-10 Hz) across all CA1 layers (s.pyr., s.r. and s.l.m.; Figure S8). Similarly, we did not find any change in the power profile at higher frequency ranges (slow gamma,

20-45 Hz; medium gamma 60-90 Hz) in either the s.r. and s.l.m. (Figure S9). The relationship between oscillations at different frequencies, expressed as phase-frequency coupling, was left intact by our manipulation (Figure S10). These results suggest that our restricted manipulation did not impair the coordinated synaptic activity in CA1 terminals supporting neural oscillations.

Theta phase precession has been seen as an organizing principle for hippocampal neural activity, even generating a temporal, phase code for animal position [17] more precise than the information contained in the firing rate. A number of potential network mechanisms have been proposed [25, 20], each with implications for hippocampal computations. Here, by making use of a highly specific optogenetic pathway manipulation, we show instead that phase precession in CA1 may be understood as a consequence of the temporal distribution of two inputs, from CA3 and EC LIII [7]. Namely, EC LIII exerts tight control over the CA1 spiking activity in the second part of the place field and earlier phases of theta. Phase precession is observed when both early theta phase and late theta phase (for which presumably the CA3 input is sufficient) are present. Thus, our data suggests that rather than a "phase code" for position spiking, theta phase precession reflects the variability in the intensity of the two inputs to CA1, with less immediate computational implications. Even more striking is the finding that EC LIII inhibition improves the organization of theta sequences. The most parsimonious interpretation of this result is that sequence generation is internal to the hippocampus proper, and probably due to CA3-CA1 interactions. CA3 is endowed with the optimal recurrent connectivity to hold a reservoir of short-time spatial sequences, or preexisting neuronal dynamics [26], which may be passed to CA1. These spiking sequences may represent the basic units of many computations. Indeed, spikes in the first part of the place fields, more robustly supported by CA3 input, appear to have a predictive coding character [18, 27]. In contrast, the EC input seems to be extraneous to such precise temporal organization, so that its presence disrupts sequence decoding. A hypothesis compatible with our data is that EC LIII drives plasticity in CA1 carrying external information, that may be used for prediction validation. This plasticity however cannot depend on precise spike timing, but it may rely on mechanisms at a longer time scales, as it has been recently proposed [12], bridging the ≈100 ms gap between theta phases. What is then, one may ask, the role of spreading CA3 and EC inputs at different phases of the theta cycle? It is possible that it is just the by-product of the feedback dynamics among the structures that produce theta oscillations (in the hippocampus and elsewhere) [5, 19]. On the other hand, we may speculate that such arrangement in the temporal segregation of inputs may provide a time window (the late theta phase) in each theta phase where sequences can be expressed "undisturbed", favoring their readout in downstream structures. As it has been hypothesized [18, 16] the theta cycle may be separated in a phase for "encoding" (early theta phase) and a phase for "retrieval", prediction and other computations. Our data suggest a clear role for direct EC inputs in the encoding phase, suggesting a novel network architecture.

Extended data

Subjects

6 male mice were used in this study, all implanted with a Hybrid Drive [14]. All animals received the implant between 16 and 31 weeks of age. After surgical implantation, mice were individually housed on a 12-h light-dark cycle and tested during the dark period. Water and food were available *ad libitum*. All experiments were performed in accordance with the Norwegian Animal Welfare Act and the European Convention for the Protection of Vertebrate Animals used for Experimental and Other Scientific Purposes. Protocols were approved by the Norwegian Food and Safety Authority (FOTS ID 17898).

Transgenic mouse lines

We crossed two transgenic mouse lines in this study. The ECLIII-tTA driver line expressing the tetracycline transactivator (tTA) within a subpopulation of cells confined to the Entorhinal Cortex Layer III (EC LIII) was made using the Enhancer Driven Gene Expression method with enhancer LEC13-8A, mapped to the Dok5 gene [3]. This ECLIII-tTA driver line was crossed to a tTA-dependent JAWS-tetO line generated as follows: transgene JAWS-GFP-ER2 (Addgene plasmid #65016) was cloned with restriction enzyme BamHI and NotI into an injection plasmid containing TRE tight 2 promoter (Clontech, now Takara Bio International). The injection plasmid was linearized by enzyme digestion to keep the relevant elements but remove the bacterial elements of the plasmids. Linearized DNA was run on a 1% agarose gel and isolated using a Zymoclean Gel DNA Recovery Kit (Zymo research, D4001). The resulting final injection construct thus consisted of a TREtight2 promoter followed by JAWS-GFP-ER2 sequences, WPRE element and SV40 polyA (TRE-Tight-2-tetO-JAWS-GFP-ER-WPRE-SV40). Fertilized oocytes from strain B6D2F1 x B6D2F1 were injected with the purified DNA. Both injection constructs were generated by the Kentros group at the Kavli Institute for Systems Neuroscience and sent for pronuclear injections at the Transgenic Mouse Facility at the University of Oregon, Eugene, OR USA.

Implant device and surgical procedures

The fabrication of the Hybrid Drive was done as described earlier [14]. This version of the Hybrid Drive is equipped with a linear silicon probe and 13 tetrodes. Additionally, an optic fiber was incorporated in the design to carry out in-vivo optogenetic manipulations. The optic fiber was placed at the center of the array and glued in place at a depth of 1 mm from brain surface, sitting above the pyramidal layer $\approx 100\ \mu$m, in order to maximize the light coverage in the s.l.m. with minimal disruption of the cell layer. Mice were anaesthetized with isoflurane (5 % induction and 1-2 % maintenance). Prior to implantation, mice were given a subcutaneous injection of analgesics (Metacam, 5 mg/kg and Temgesic, 0.1 mg/kg), plus a local anaesthesia (Marcain, 1 mg/kg). Anaesthetized mice were secured in a stereotaxic frame. The skull was exposed, cleaned and dried. 3 stainless steel M0.8 screws were used to secure the drive (1 ground screw in

the frontal plate, 1 screw in the parietal plate opposite to the drive, 1 screw in the occipital plate). Using a 0.9 mm Burr drill, a craniotomy was made over the right cortex (top-left corner at AP: -1.20 mm; ML: 0.6 mm relative to bregma; bottom-right corner at AP: -2.30 mm; ML: 2.10 mm relative to bregma). The dura was removed and the array of the drive was slowly lowered into the brain with the silicon probe shaft and the optic fiber already adjusted at the final depth. To prevent cement from entering the guide tube array and the exposed brain, the craniotomy was filled with sterile Vaseline before lowering the array. The drive was cemented onto the skull using dental adhesive (Superbond C&B, Sun Medical, Japan) and tetrodes were individually lowered into the brain (5 turns - $\approx$ 900 μm). Mice were allowed to recover from surgery for at least seven days before experiments began.

Neural and behavioral data collection

Animals were transported to the recording room from post-surgery day 3 and electrophysiological signals were studied during a rest session in the home cage. Each day, tetrodes were lowered individually in 45/60 μm steps (1/2 of a screw turn), until clear physiological markers for the CA1 pyramidal layer were discernible (sharp wave ripple complexes during sleep or theta during locomotion). The target location was usually reached in 10 days. Electrophysiological signals from the silicon probe contacts helped to refine the final position of the tetrodes.

Electrophysiological data were recorded with an Open Ephys acquisition board [23]. Signals were referenced to ground, filtered between 1 and 7500 Hz, multiplexed, and digitized at 30 kHz on the headstages (RHD2132, Intan Technologies, USA). Digital signals were transmitted over two custom 12-wire cables (CZ 1187, Cooner Wire, USA) that were counter-balanced with a pulley-system. Waveform extraction and automatic clustering were performed using Dataman (https://github.com/wonkoderverstaendige/dataman). Clustered units were manually curated using the MClust toolbox. During all experiments, video data was recorded using a video camera (The Imaging Source, DMK 37BUX273) mounted above the linear track.

Behavioral paradigm

Each behavioural session was preceded and followed by a 60-minute rest session in the animal's home cage ("Pre sleep" and "Post sleep"). Mice were placed at one end of a 1-meter long track and trained to run to the other end, collecting a food reward (a piece of Weetos chocolate cereal). Following the animal's consumption of the reward, a new one was placed at the opposite end. A lap was defined as an end-to-end run in which the animal's body started at the first 10 cm of the track and finished at the other end without returning to its starting place. When the animals consistently carried out the task with an high number of laps, after approximately 10 days of consecutive training, the session with the optogenetic manipulation was carried out. Recordings typically lasted between 20 and 30 minutes. Animals were familiar with the recording room and the proximal and distal cues around the linear track. Mice were not food nor water deprived.

Optogenetics

For optical silencing of EC LIII projections to s.l.m. of the hippocampal CA1 subregion, an optic fiber (core diameter: 100 μm, numerical aperture: 0.37, Doric Lenses) with a cone termination was incorporated in the Hybrid Drive and unilaterally implanted in the right hemisphere at a depth of 1 mm. Optogenetic stimulation was performed by the delivery of continuous red light (640 nm, 20 mW at fiber tip) by a diode laser (Coherent Obis LX 1185054). Laser power was carefully curated to obtain sufficient irradiance in s.l.m. while avoiding excessive, detrimental effects. The onset and offset of light delivery were triggered as the animal left from one end and upon arrival at the other end of the linear track, respectively. Each lap with light stimulation was followed by a non-stimulated lap, providing an internal control for the effect of light stimulation. Optogenetic silencing sessions were performed once the mice proficiently performed on the linear track.

Histology

Following the end of experiments, tetrodes were left untouched. Animals were euthanized using an overdose of pentobarbital, and perfused transcardially with RNase free 4% paraformaldehyde in PBS. The brains were extracted and stored in RNase free 4% paraformaldehyde for 24 hours before being transferred into RNase free 30% sucrose for 2 days. For each animal, the left hemisphere was used to monitor transgene expression and the right hemisphere was used to verify the location of tetrodes, silicone probe and optic fiber. Both hemispheres were sectioned sagitally in 30 μm thick slices using a Cryostat (Fisher Scientific, Cryostar NX70). Sections were divided into 6 series and stored in a $-$ 80°C freezer. For the identification of recording sites and the position of the optic fiber, the tissue was stained with Cresyl violet. The slides were coverslipped and brightfield images were taken using a scanner (Zeiss Axio Scan.Z1, Germany) at a magnitude of 5x. Tracts were assigned to the Allen Mouse Brain Atlas and visualised in 3D using MeshView (https://www.nesys.uio.no/MeshView/). To validate transgene expression, the tissue was stained using both fluorescent in situ hybridization and immunohistochemistry. The sections were hybridized overnight at 62 °C with a FITC-riboprobe for GFP (2.5:1200; Roche, Cat. 11685619910). Next, the sections were washed with a tris-buffered saline with tween (TBST) solution and incubated in a blocking solution (600 µl MABT, 200 µl sheep serum, 200 µl 10 % blocking reagent; Roche, Cat. 285 No. 11096176001) at room temperature for 4 hours. The blocking solution was replaced with anti-FITC-POD (1:1000) and the sections were left to incubate overnight at room temperature. The following day, the tissue was washed with a TBST solution before the fluorescein signal was developed using Tyr-FL (1:50, PerKinElmer kit) for 45 mins at room temperature, then washed in a TBST solution. The sections were then stained for PCP4 and NeuN with antibodies. The tissue was washed with 1X phosphate-buffered saline (PBS) (2 x 10 mins), placed in a permeabilisation buffer (1X PBS + 0.3 % Triton-X100, 10 mins) and preincubated in a blocking buffer (1x PBS + 0.3 % Triton X-100 + 3 % bovine serum, BSA, 1 hour). The sections were then incubated at room temperature for 48 hours with primary antibodies: Rabbit anti-PCP4 (1:300, Sigma, HPA005792) and Guinea Pig anti-NeuN

(1:1000, Millipore, ABN90P) diluted in a solution of 1x PBS + 0.3 % Triton X-100 + 3 % BSA. Following primary antibody processing, sections were washed with 1X PBS + 0.3 % Triton X-100 + 3 % BSA (3 x 10 mins), then incubated at room temperature overnight with secondary antibodies: Goat anti-Rabbit Alexa Fluor 546 (1:400, Life technologies, A11010) and Goat anti-Guinea pig Alexa Fluor 647 (1:400, Life technologies, A21450) diluted in a solution of 1X PBS + 0.1 % Triton + 1 % BSA. The slides were coverslipped and images were taken using a scanner (Zeiss Axio Scan.Z1, Germany) at a magnitude of 5x.

Automated cell counting

Cell counting was performed on one series of brain slices per animal. The EBRAINS semi-automated workflow QUINT ([29, 13, 21]; https://ebrains.eu/service/quint/) was used for cell quantification. The brain slices were registered to the Allen Mouse Brain Atlas (http://www.brain-map.org/) using the QuickNII software. Anatomical boundaries from the atlas were fine-tuned to fit the data using non-linear adjustments in VisuAlign (https://www.nitrc.org/projects/visualign/). Cells were extracted by using machine-learning image segmentation toolkit ilastik. Finally, Nutil Quantifier was used to quantify and assign anatomical locations to labelled cells obtained by segmentation of brain images.

Place Cell Identification

We first selected putative excitatory pyramidal cells using their auto-correlograms, firing rates and waveform information. Specifically, pyramidal cells were classified as such if they had a mean firing rate <8 Hz and the average first moment of the auto-correlogram (i.e., the mean value) occurring before 8 milliseconds. Only cells classified as pyramidal cells were used for further place cell analysis. Place cells were defined applying a combination of different criteria. All analysis were performed on speed-filtered activity, after removing periods in which the animal speed was smaller than 3 cm/s. Only cells with an average activity above 0.3 Hz were taken into account. Then for each of these cells, the Skaggs information per second $I = \sum_x \xi(x) log \frac{\xi(x)}{<\xi>_x}$ was compared to the distribution of information values resulting from randomly shuffling cell spike times. A cell passed the selection if its Skaggs information was significantly higher than the ones of the surrogate distribution. Last, only place cells with peak firing rate higher than 1 Hz were kept for further analysis.

Place Cell Classification

Spikes were filtered both in speed (>3cm/s) and in position, by taking only those emitted within the boundaries of the cell place field. For each place cell, a 'Theta Score' [15] was calculated as follows: Theta Score = Precession Score - Locking Score. For the Precession Score we used a circular-linear correlation to measure the degree of dependency between the spike phase and the position within the field. For the Locking Score we computed the length of the Reyleigh vector associated to the distribution of spike phases with respect to the instantaneous theta phase. Each measure produced

a score between 0 and 1, with 1 denoting perfect phase-position relation or perfect phase locking. Negative Theta Score values indicate that spikes probability are mostly modulated by specific phases of theta ('phase locking cells'), while positive Theta Scores suggest a substantial presence of phase precession ('phase precessing cells').

Place Cell Properties

Place cell properties were calculated using a Generalized Linear Model (GLM; described in detail in [15]) to infer the spike probability of each place field given i) the position within the place field; ii) the instantaneous theta phase and iii) the instantaneous power in a specific gamma range and layer. In all our analysis, we considered a partition of the environment in bins of 2.5 cm. Place fields were isolated as continuous regions in the rate map with rate higher than 20 % of the cell maximum activity. Spatial mean firing rate was calculated integrating these probabilities over the other variables. Spatial firing rate of each cell was calculated within each condition and separately for Laser OFF and Laser ON. As place field center we took the bin within the place field with highest firing rate. The effect of speed on the firing probabilities was addressed in a similar manner, by including the instantaneous velocity of the animal as a further covariate in the GLM .

Neural data analysis on oscillations

Before applying other analysis, continuous (LFP) signals were down-sampled to 1 kHz. Then, LFP across the 16 contacts was used to compute the corresponding Current Source Density signal. This transformation is based on computing the discrete laplacian along the probe axis (that is along the direction running through CA1 layers). The resulting CSD signal is limited to 14 channels (16 minus the 2 extremes). Power spectral density (PSD) estimates were calculated across the frequency range 30–150 Hz using the pwelch function in Matlab, for each condition (Laser OFF vs. Laser ON) separately. We used the CSD signal to compute the phase-amplitude coupling strength between a reference theta oscillation and faster oscillations, in a [15-150] Hz range. we first applied a wavelet transform to obtain the CSD analytical signal over time and then we tracked the evolution of the phase-amplitude couplings across different layers and frequencies [15]. For each of the identified main gamma frequency ranges (slow [20-45] Hz and medium [60-90] Hz) we extracted layer-specific coupling strength and phase range of frequencies. Theta oscillation reference was generally taken from the s.l.m., where theta modulation of the LFP is strongest.

Gamma Coefficient

The instantaneous balance between the power in the slow gamma ($P_{Slow}(t)$) and medium gamma ($P_{Med}(t)$) frequency range was computed as follow. First, both the slow gamma power and medium gamma power during running periods were separately z-scored. Second, a power-ratio score, spanning the [-1 1] interval was computed as:

$$\gamma = \frac{P^z_{Slow}(t) - P^z_{Med}(t)}{P^z_{Slow}(t) - P^z_{Med}(t)}$$

so that a value of -1 would correspond to total medium gamma domination and +1 to slow gamma completely dominating.

Generalized-Linear Model (GLM)

The GLM analysis was carried out (separately for periods with and without Laser manipulation) as previously described in [15].

Pairwise Spike Timing correlations

Pairwise correlations analysis was carried out (separately for periods with and without Laser manipulation) as previously described in [15].

Statistics

Data analyses were performed using custom MATLAB scripts (The Math Works). Paired and unpaired t- tests and Kolmogorov-Smirnov tests were performed using standard built-in MATLAB functions. 2-D Kolmogorov-Smirnov test was performed using custom code based on the Peacock algorithm. All tests were two-tailed, except where stated otherwise.

Acknowledgments

We thank Morgane Audrain for help with the 3D illustration of the Hybrid Drive, Jordan Carpenter, the Kentros and Battaglia labs for comments on the manuscript and helpful discussions at different stages of the project. This work was supported by the European Union's Horizon 2020 research and innovation program (MGate, grant agreement no. 765549; M.G., O.C., C.K. and F.P.B.), the European Research Council (ERC) Advanced Grant "REPLAY-DMN" (grant agreement no. 833964; F.P.B.), and European Union's Horizon 2020 Research and Innovation Program Grant "BrownianReactivation" (grant agreement no. 840704; F.S.), FRIPRO ToppForsk grant Enhanced Transgenics (90096000) of the Research Council of Norway (O.C., Q.Z. and C.K), the Kavli Foundation (O.C., Q.Z. and C.K), the Centre of Excellence scheme of the Research Council of Norway—Centre for Biology of Memory and Centre for Neural Computation (O.C., Q.Z. and C.K), The Egil and Pauline Braathen and Fred Kavli Centre for Cortical Microcircuits (O.C., Q.Z. and C.K), and the National Infrastructure scheme of the Research Council of Norway—NORBRAIN (O.C., Q.Z. and C.K).

Author contributions

Conceptualization: M.G., O.C., F.S., C.K. and F.P.B.; Investigation and Data Curation: M.G.and O.C.; Methodology and Software: M.G, O.C., Q.Z., F.S., C.K. and F.P.B.; Resources: C.K. and F.P.B.; Formal Analysis and Visualization: F.S. and M.G.; Writing – Original Draft: M.G., O.C. and F.P.B.; Writing – Review & Editing: M.G., O.C., F.S., C.K. and F.P.B.; Supervision and Funding Acquisition: F.S., C.K. and F.P.B.

Ethics declarations

The authors declare no competing interests.

References

[1] O. J. Ahmed and M. R. Mehta. Running speed alters the frequency of hippocampal gamma oscillations. 32(21):7373–7383. Publisher: Society for Neuroscience Section: Articles.

[2] K. W. Bieri, K. N. Bobbitt, and L. L. Colgin. Slow and fast gamma rhythms coordinate different spatial coding modes in hippocampal place cells. 82(3):670–681.

[3] S. Blankvoort, M. P. Witter, J. Noonan, J. Cotney, and C. Kentros. Marked diversity of unique cortical enhancers enables neuron-specific tools by enhancer-driven gene expression. 28(13):2103–2114.e5.

[4] V. H. Brun, M. K. Otnass, S. Molden, H.-A. Steffenach, M. P. Witter, M.-B. Moser, and E. I. Moser. Place cells and place recognition maintained by direct entorhinal-hippocampal circuitry. 296(5576):2243–2246.

[5] G. Buzsáki and E. Moser. Memory, navigation and theta rhythm in the hippocampal-entorhinal system. 16:130–8.

[6] H. O. Cabral, M. Vinck, C. Fouquet, C. M. A. Pennartz, L. Rondi-Reig, and F. P. Battaglia. Oscillatory dynamics and place field maps reflect hippocampal ensemble processing of sequence and place memory under NMDA receptor control. 81(2):402–415.

[7] F. S. Chance. Hippocampal phase precession from dual input components. 32(47):16693–16703. Publisher: Society for Neuroscience Section: Articles.

[8] A. S. Chuong, M. L. Miri, V. Busskamp, G. A. C. Matthews, L. C. Acker, A. T. Sørensen, A. Young, N. C. Klapoetke, M. A. Henninger, S. B. Kodandaramaiah, M. Ogawa, S. B. Ramanlal, R. C. Bandler, B. D. Allen, C. R. Forest, B. Y. Chow, X. Han, Y. Lin, K. M. Tye, B. Roska, J. A. Cardin, and E. S. Boyden. Noninvasive optical inhibition with a red-shifted microbial rhodopsin. 17(8):1123–1129.

[9] L. L. Colgin, T. Denninger, M. Fyhn, T. Hafting, T. Bonnevie, O. Jensen, M.-B. Moser, and E. I. Moser. Frequency of gamma oscillations routes flow of information in the hippocampus. 462(7271):353–357.

[10] G. Dragoi and G. Buzsáki. Temporal encoding of place sequences by hippocampal cell assemblies. 50(1):145–157.

[11] D. J. Foster and M. A. Wilson. Hippocampal theta sequences. 17(11):1093–1099. _eprint: https://onlinelibrary.wiley.com/doi/pdf/10.1002/hipo.20345.

[12] C. Grienberger and J. C. Magee. Entorhinal cortex directs learning-related changes in CA1 representations. 611(7936):554–562. Number: 7936 Publisher: Nature Publishing Group.

[13] N. E. Groeneboom, S. C. Yates, M. A. Puchades, and J. G. Bjaalie. Nutil: A pre- and post-processing toolbox for histological rodent brain section images. 14.

[14] M. Guardamagna, R. Eichler, R. Pedrosa, A. A. Aarts, A. F. Meyer, and F. Battaglia. The hybrid drive: a chronic implant device combining tetrode arrays with silicon probes for layer-resolved ensemble electrophysiology in freely moving mice.

[15] M. Guardamagna, F. Stella, and F. P. Battaglia. Heterogeneity of network and coding states in mouse CA1 place cells. 42(2). Publisher: Elsevier.

[16] M. E. Hasselmo and C. E. Stern. Theta rhythm and the encoding and retrieval

of space and time. 85(0):656–666.

[17] J. Huxter, N. Burgess, and J. O'Keefe. Independent rate and temporal coding in hippocampal pyramidal cells. 425(6960):828–832. Bandiera_abtest: a Cg_type: Nature Research Journals Number: 6960 Primary_atype: Research Publisher: Nature Publishing Group.

[18] J. Lisman and A. Redish. Prediction, sequences and the hippocampus. 364(1521):1193–1201. Publisher: Royal Society.

[19] K. Mizuseki, K. Diba, E. Pastalkova, and G. Buzsáki. Hippocampal CA1 pyramidal cells form functionally distinct sublayers. 14(9):1174–1181.

[20] J. O'Keefe and M. L. Recce. Phase relationship between hippocampal place units and the EEG theta rhythm. 3(3):317–330. _eprint: https://onlinelibrary.wiley.com/doi/pdf/10.1002/hipo.450030307.

[21] M. A. Puchades, G. Csucs, D. Ledergerber, T. B. Leergaard, and J. G. Bjaalie. Spatial registration of serial microscopic brain images to three-dimensional reference atlases with the QuickNII tool. 14(5):e0216796. Publisher: Public Library of Science.

[22] M. I. Schlesiger, C. C. Cannova, B. L. Boublil, J. B. Hales, E. A. Mankin, M. P. Brandon, J. K. Leutgeb, C. Leibold, and S. Leutgeb. The medial entorhinal cortex is necessary for temporal organization of hippocampal neuronal activity. 18(8):1123–1132. Bandiera_abtest: a Cg_type: Nature Research Journals Number: 8 Primary_atype: Research Publisher: Nature Publishing Group Subject_term: Neural circuits Subject_term_id: neural-circuit.

[23] J. H. Siegle, A. C. López, Y. A. Patel, K. Abramov, S. Ohayon, and J. Voigts. Open ephys: an open-source, plugin-based platform for multichannel electrophysiology. 14(4):045003.

[24] W. E. Skaggs, B. L. McNaughton, M. A. Wilson, and C. A. Barnes. Theta phase precession in hippocampal neuronal populations and the compression of temporal sequences. 6(2):149–172. _eprint: https://onlinelibrary.wiley.com/doi/pdf/10.1002/%28SICI%291098-1063%281996%296%3A2%3C149%3A%3AAID-HIPO6%3E3.0.CO%3B2-K.

[25] M. V. Tsodyks, W. E. Skaggs, T. J. Sejnowski, and B. L. McNaughton. Population dynamics and theta rhythm phase precession of hippocampal place cell firing: A spiking neuron model. 6(3):271–280.

[26] M. Valero, I. Zutshi, E. Yoon, and G. Buzsáki. Probing subthreshold dynamics of hippocampal neurons by pulsed optogenetics. 375(6580):570–574. Publisher: American Association for the Advancement of Science.

[27] M. Wang, D. J. Foster, and B. E. Pfeiffer. Alternating sequences of future and past behavior encoded within hippocampal theta oscillations. 370(6513):247–250. Publisher: American Association for the Advancement of Science.

[28] M. P. Witter, F. G. Wouterlood, P. A. Naber, and T. Van Haeften. Anatomical organization of the parahippocampal-hippocampal network. 911:1–24.

[29] S. C. Yates, N. E. Groeneboom, C. Coello, S. F. Lichtenthaler, P.-H. Kuhn, H.-U. Demuth, M. Hartlage-Rübsamen, S. Roßner, T. Leergaard, A. Kreshuk, M. A. Puchades, and J. G. Bjaalie. QUINT: Workflow for quantification and spatial analysis of features in histological images from rodent brain. 13.

[30] C. Zheng, K. W. Bieri, Y.-T. Hsiao, and L. L. Colgin. Spatial sequence coding differs during slow and fast gamma rhythms in the hippocampus. 89(2):398–408.

[31] I. Zutshi, M. Valero, A. Fernández-Ruiz, and G. Buzsaki. Extrinsic control and intrinsic computation in the hippocampal CA1 circuit. 110(4):658–673.e5.

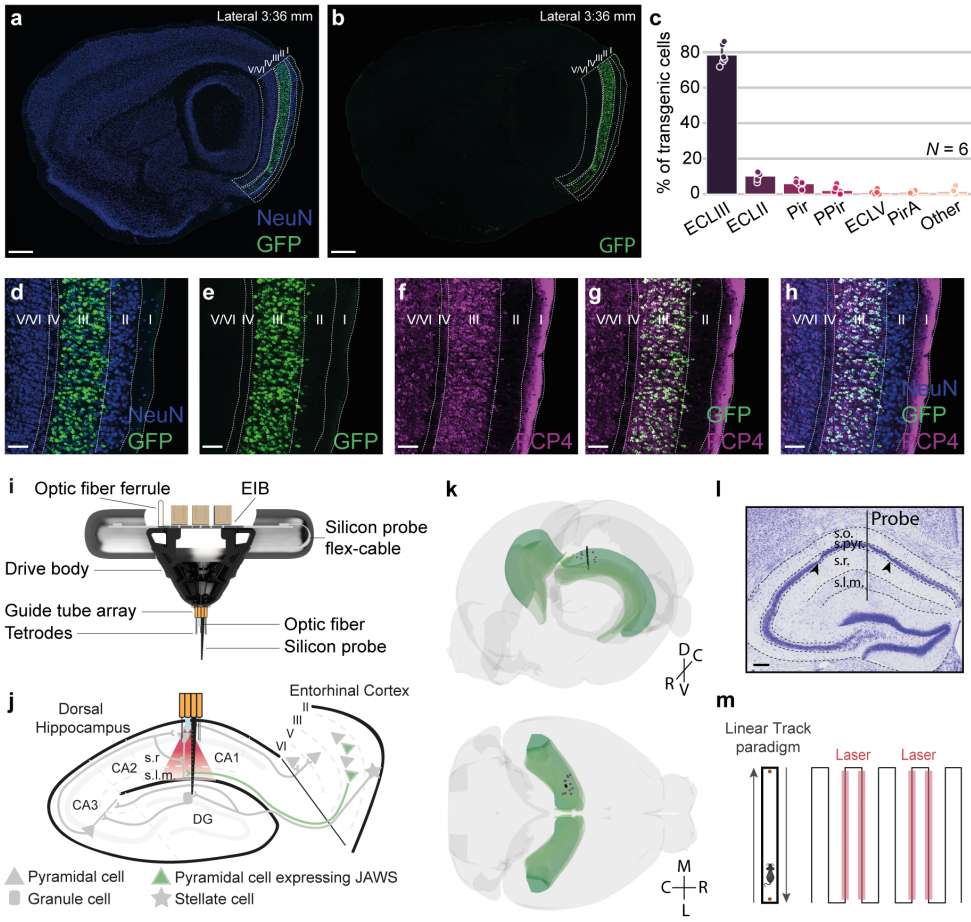

Fig. 1 Novel transgenic cross for optogenetic manipulation of entorhinal cortex layer III and layer resolved ensemble electrophysiology in CA1. (a) Fluorescent in situ hybridization of a sagittal brain slice targeting the transgene GFP (green), fused to the JAWS opsin in the EC LIII-EDGE x JAWS mouse cross. Expression is largely restricted to Entorhinal Cortex Layer III (EC LIII). Counterstain NeuN (blue). Scale bar: 500 μm. (b) Same as (A) without the NeuN counterstain. (c) Percentage of GFP labelled neurons by brain region. EC LIII, entorhinal cortex layer III; EC LII, entorhinal cortex layer II; Pir, piriform area; PPir, postpiriform transition area; EC LV, entorhinal cortex layer V; PirA, piriform-amygdala area. (d-h) High magnification images of dorsal MEC showing NeuN (blue), GFP (green) and PCP4 (violet) expression. Scale bar: 100 μm. (i) Simplified schematic of the Hybrid Drive, with optic fiber. (j) Schematic of the entorhinal-hippocampal system illustrating the Hybrid Drive implant in CA1 and specific expression of the JAWS opsin to a subset of EC LIII pyramidal cells. The Hybrid Drive, composed of 13 tetrodes, an optic fiber and a silicone probe, was implanted in dorsal CA1 and enabled the recording of neural activity throughout the layers of CA1 as well as optical manipulation of the direct projection conveyed from EC LIII to *stratum lacunosum moleculare* (s.l.m.). s.r., *stratum radiatum.* (k) 3D reconstruction from histology of tetrode (black dots) and silicone probe (black shank) tracts. The hippocampal formation is depicted in green. D, dorsal; V, ventral; C, caudal; R, rostral. (l) Representative Nissl staining showing tetrode (arrows) and silicone probe (bar) tracts from the Hybrid Drive implant. Scale bar: 100 μm. s.o., *stratum oriens*; s.pyr., *stratum pyramidale.* (m) Representative schematics of the linear track paradigm.

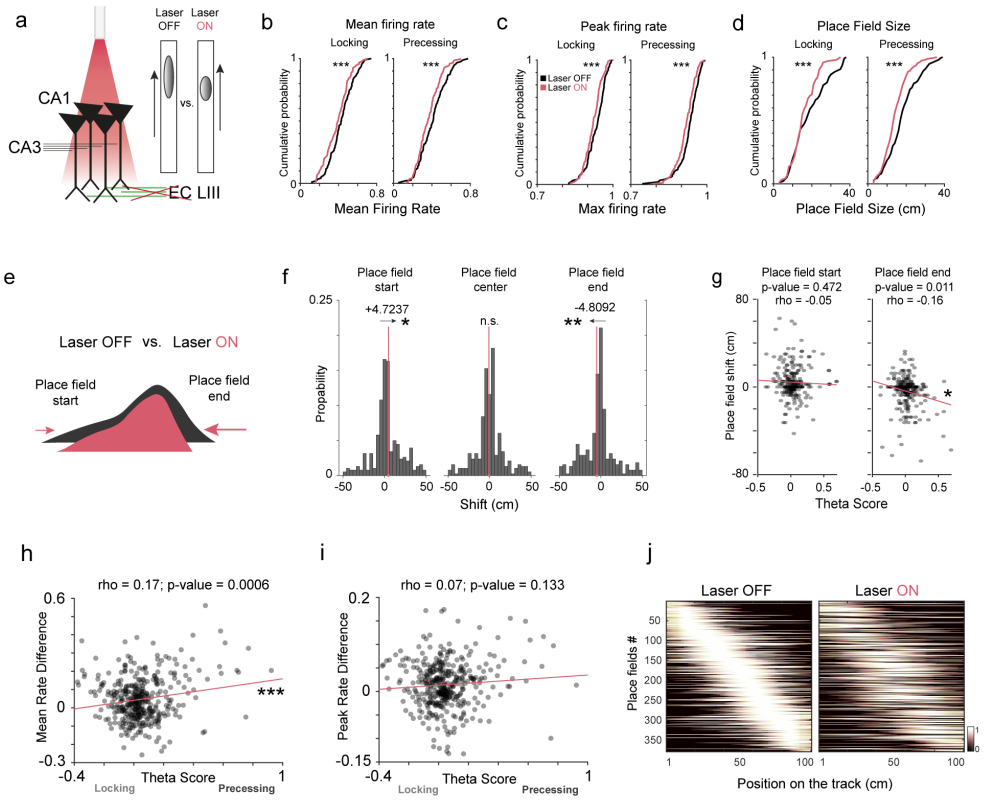

Fig. 2 Spatial coding in CA1 does not rely on sustained EC LIII direct input. (a) Schematic illustration of the optogenetic manipulation, selectively blocking the input from EC LIII, reaching the distal dendrites of CA1 pyramidal cells in the s.l.m.. (b) Distributions of normalized mean firing rate in Laser OFF and Laser ON conditions for phase locking and phase precessing cells. All animals (N=6), all sessions (n=11). Only cells with a stable place field center (shift<20 cm) were considered for this analysis (n=245). Significant differences for both populations. Kolmogorov–Smirnov test, Locking: $p<10e^{-04}$; Precessing: $p<10e^{-06}$. (c) Distributions of normalized peak firing rate in Laser OFF and Laser ON conditions for phase locking and phase precessing cells. All animals (n=6), all sessions (n=11). Only cells with a stable place field center (shift<20 cm) were considered for this analysis (n=245). Significant differences for both populations. Kolmogorov–Smirnov test, Locking: p=0.009; Precessing: p=0.001 (d) Distributions of place field sizes in Laser OFF and Laser ON conditions for phase locking and phase precessing cells. All animals (n=6), all sessions (n=11). Same cell population as in (c). Significant differences for both populations. Kolmogorov–Smirnov test, Locking: p=0.0005; Precessing: $p<10e^{-07}$. (e) Representative illustration of the effects of EC LIII optogenetic manipulation on place field shape. (f) Amount of shift (in cm) on the linear track between Laser OFF and Laser ON conditions, for the place field start, place field center and place field end. Both forward and backward shifts are statistically different from within-condition controls (Kolmogorov–Smirnov one-sided test; mean shift start =+4.72 cm, p=0.02; mean shift end =-4.80 cm, p=0.006). (g) Shift of the place field start (left panel) and end (right panel) as a function of the theta score. Larger shift of the place field end for fields with higher theta score (steeper phase precession; Spearman's rho = -0.16, p-value = 0.011). (h) Mean rate difference as a function of the theta score. Higher mean firing rate for place fields with higher theta score (steeper phase precession; Spearman's rho = 0.17, p-value = 0.0006). (i) Peak rate difference as a function of the theta score. No differences across the population (Spearman's rho = 0.07, p-value = 0.133). (j) All place fields (rows) recorded during experiments (n=380) sorted by their peak firing position during laser OFF on the linear track (columns). *p < 0.05, **p < 0.01, ***p < 0.001.

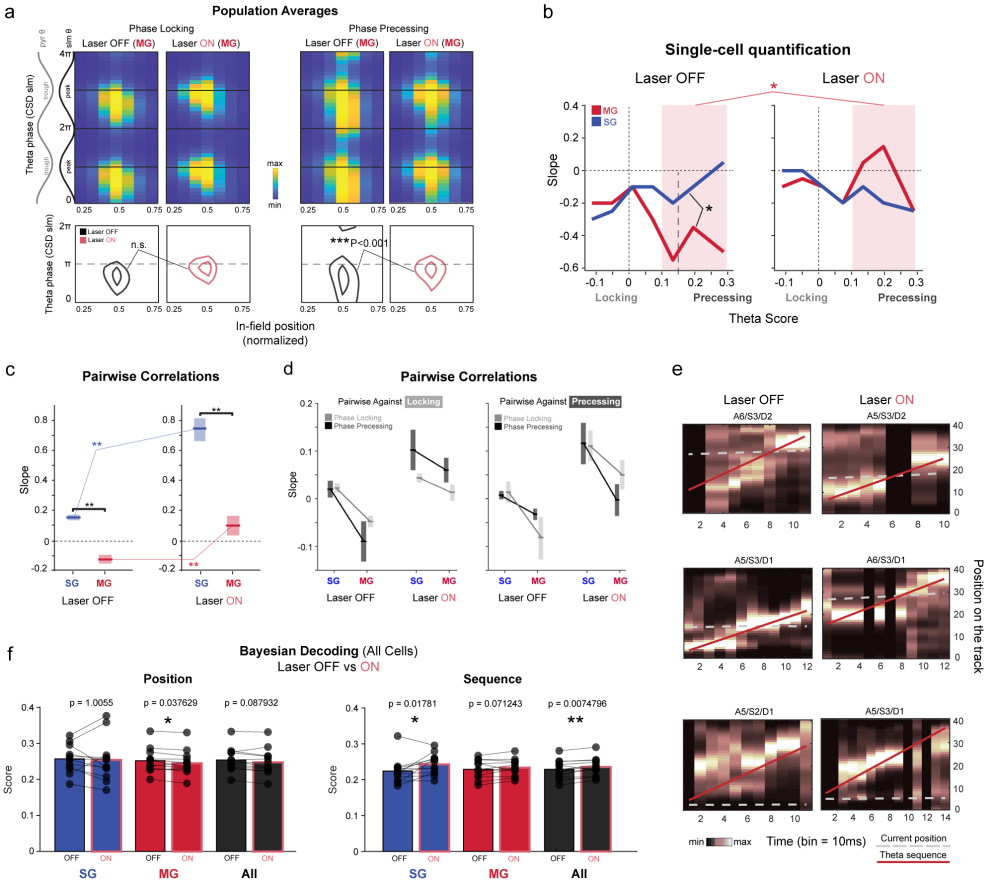

Fig. 3 Effects of EC LIII input inhibition on CA1 temporal coding processes. SG = slow gamma (20-45Hz); MG = medium gamma (60-90Hz). (a) Top row, global average of the in-field spike probability during medium gamma network states, in Laser OFF (left panel) and Laser ON (right panel) runs, for both phase locking and phase precessing cells. Bottom row, contour of regions with highest density of spikes for both phase locking and phase precessing cells, curves correspond to 85 % and 95 % of the peak value of spike density (same data as top row panels). 2-Dimensional Kolmogorov–Smirnov test for spike densities, p-value<0.001). All animals (N=6), all sessions (n=11). (b) Phase-position slope values plotted against the Theta Score values for each individual cell, as a function of slow-medium gamma balance. Laser OFF left panel, Laser ON right panel. All animals (N=6), all sessions (n=11). (c) Place field distance vs phase distance regression for different gamma coefficients (slow gamma and medium gamma) and Laser conditions (OFF and ON). All comparisons are statistically significant. Kolmogorov–Smirnov test, p<0.01. (d) Spatio-temporal pairwise spike correlation computed for cell pairs either within the same cell group or across groups, as a function of the instantaneous gamma balance (slow and medium gamma) and the Laser conditions (OFF and ON). (e) Comparison of mean positional and sequential scores between different gamma conditions (slow gamma in blue, medium gamma in red, all periods in black). Paired t test. Statistical values in order of appearance. Position: p = 1.0055, p = 0.037629, p = 0.087932. Sequence: p = 0.01781, p = 0.071243, p = 0.0074796. (f) Examples of encoded position (y axis) reconstruction over an entire theta cycle (x axis, 1 bin = 10 ms). Black-white color scale: posterior probability from Bayesian decoding. Dotted grey line: real position of the animal, used to compute the amount of local coding as the probability density around the line. Red line: best positive-slope fit of probability distribution, used as an estimation of sequential non-local cell activation. *p < 0.05, **p < 0.01.

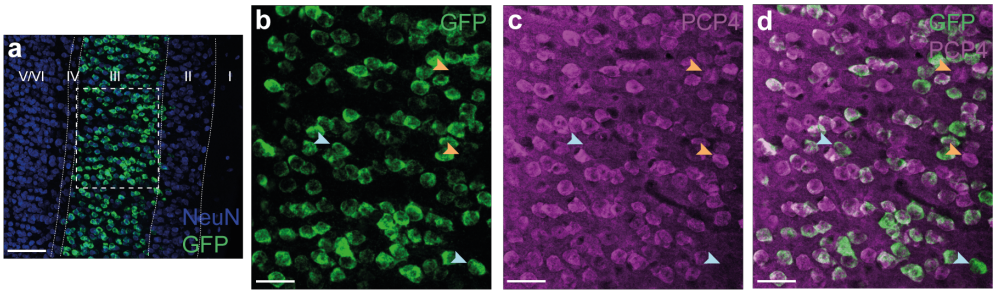

Fig. S1 Expression of the JAWS opsin is largely specific to EC LIII excitatory neurons. (a) Fluorescent In Situ Hybridization targeting the transgene GFP and NeuN. Scale bar: 100 μm. (b-d) Large majority of GFP/opsin expressing cells overlap with PCP4+ cells, marker for EC LIII neurons. Light blue arrows: example GFP+/PCP4- cells. Orange arrows: GFP-/PCP4+ cells. Scale bar: 50 μm.

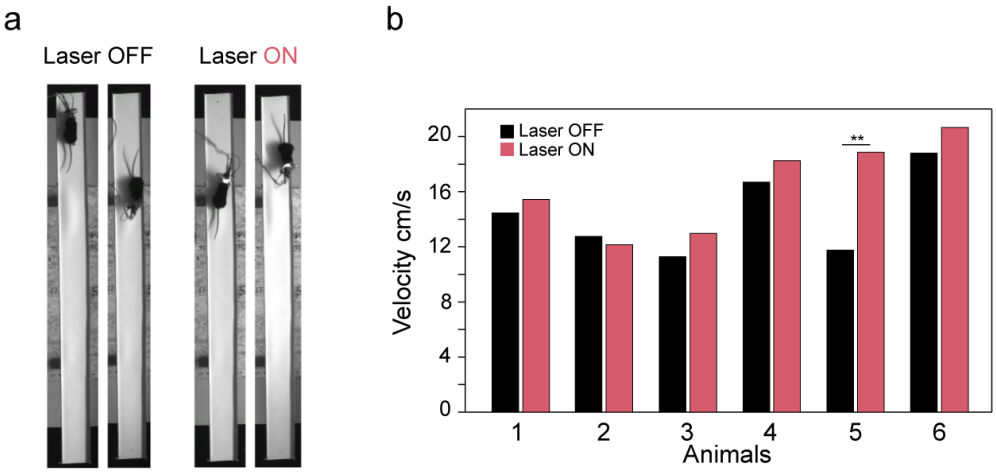

Fig. S2 Velocity performances during the goal-directed linear track task. (a) Examples of mice implanted with a Hybrid Drive in the linear track task during either Laser OFF or Laser ON runs, for both running directions. (b) Velocity performances across conditions. Only Animal 5 displayed faster performances during Laser ON trials ($p<0.01$; t-test).

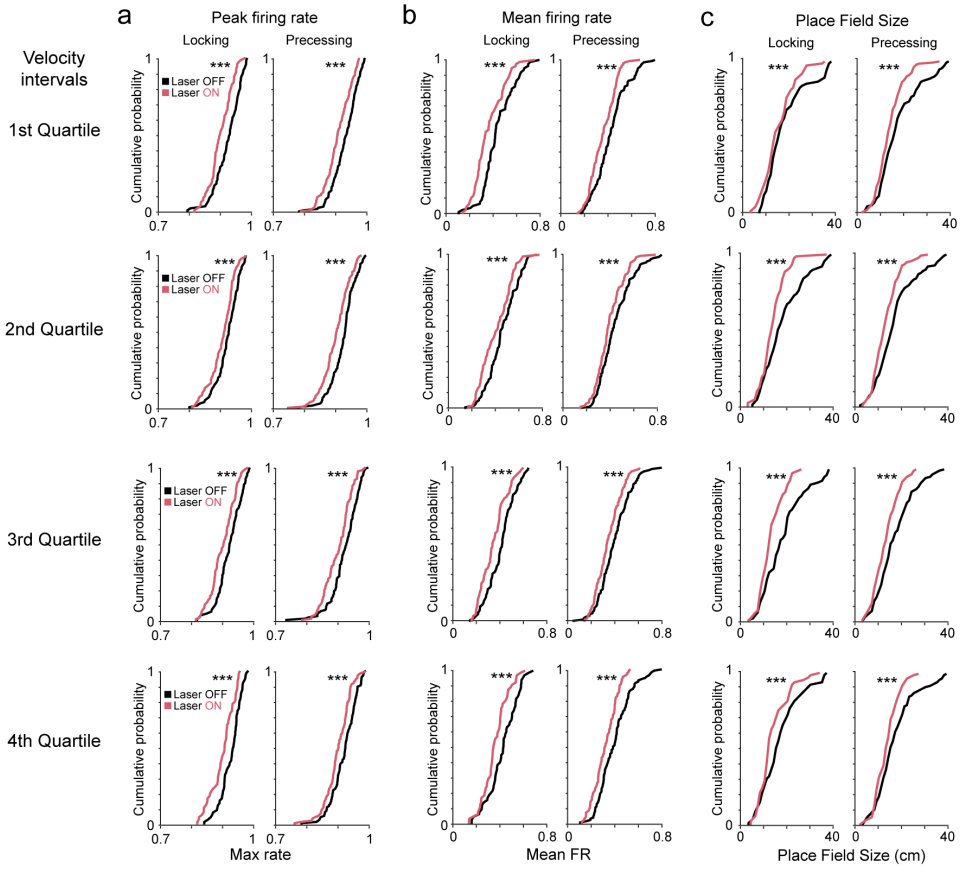

Fig. S3 Rate and place coding properties across velocity intervals. (a-c) Distributions of normalized peak firing rate, mean firing rate and place field size respectively, across different velocity intervals. All comparison are statistically significant (p<0.001; Kolmogorov–Smirnov test for all conditions all comparisons). All animals (N=6), all sessions (n=11). Same amount of data in each velocity interval. ***p ¡ 0.001

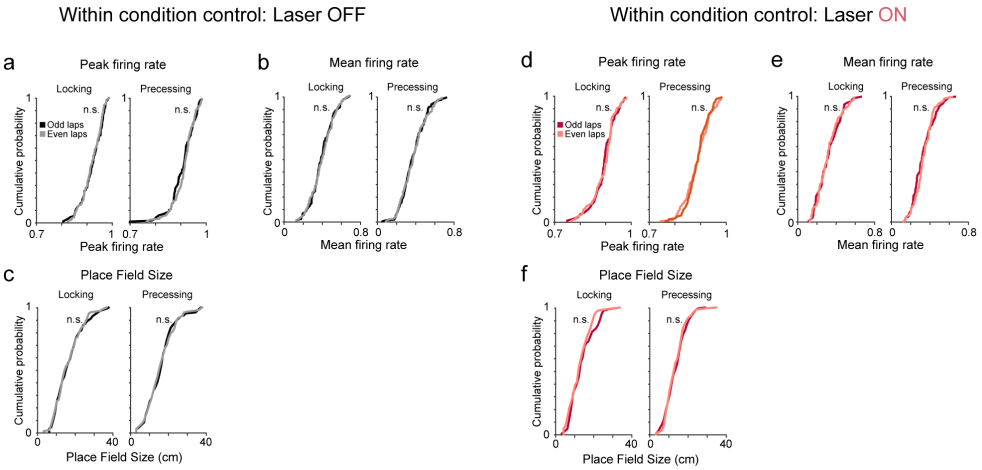

Fig. S4 Rate coding properties within conditions. (a-c) Distributions of normalized peak firing rate, mean firing rate and place field size, respectively; using only within conditions data (Odd and Even laps for Laser OFF and Laser ON separately). No significant differences were found ($p>0.05$; Kolmogorov–Smirnov test for all conditions all comparisons). All animals (N=6), all sessions (n=11). (d-f) Same thing but using Odd and Even laps within the Laser ON condition. No significant differences were found ($p>0.05$; Kolmogorov–Smirnov test for all conditions all comparisons). All animals (N=6), all sessions (n=11).

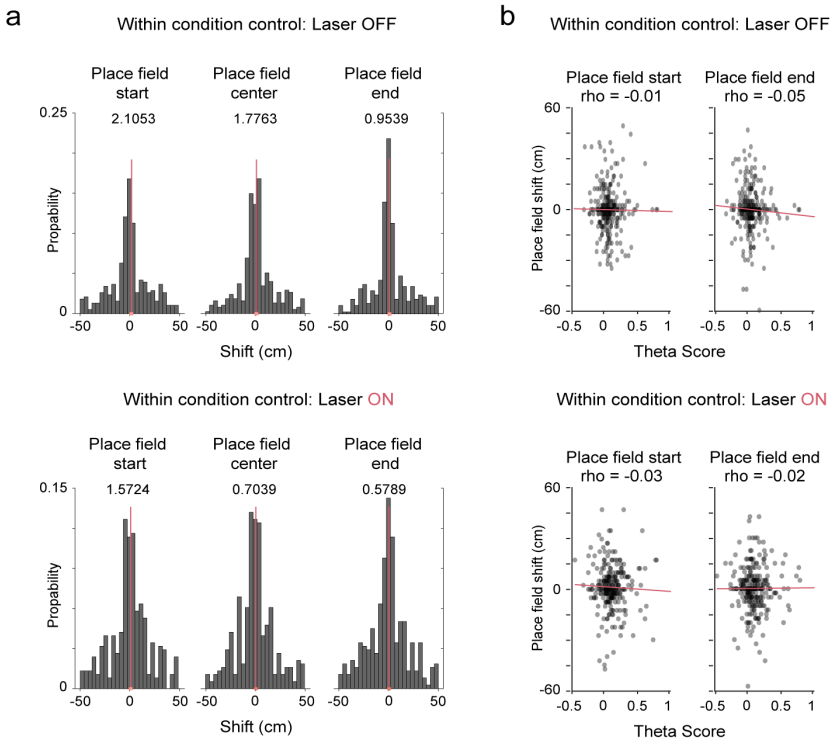

Fig. S5 Changes in place field shape within conditions. (a) Shift on the linear track (in cm) for the place field start, place field center and place field end using within conditions data (Odd and Even laps for Laser OFF and Laser ON separately) (b) Shift of the place field start and end as a function of the Theta Score, using within conditions data (Odd and Even laps for Laser OFF and Laser ON separately).

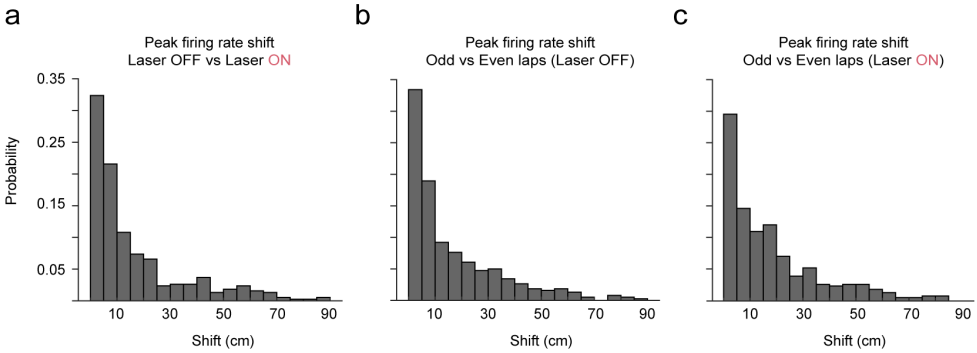

Fig. S6 Remapping dynamics across conditions. (a) Amount of shift of the place field center (defined as peak firing rate) between the Laser OFF and Laser ON conditions. Mean value = 15.5 cm. All animals (N=6), all sessions (n=11). (b) Same as in (A), but between Odd and Even laps in the Laser OFF condition. Mean value = 15.6 cm. (c) Same as in (A), but between Odd and Even laps in the Laser ON condition. Mean value = 17.0 cm. Similar distributions across and within conditions indicate that the movements of the place field center are due to intrinsic instability of the place fields, common to all conditions.

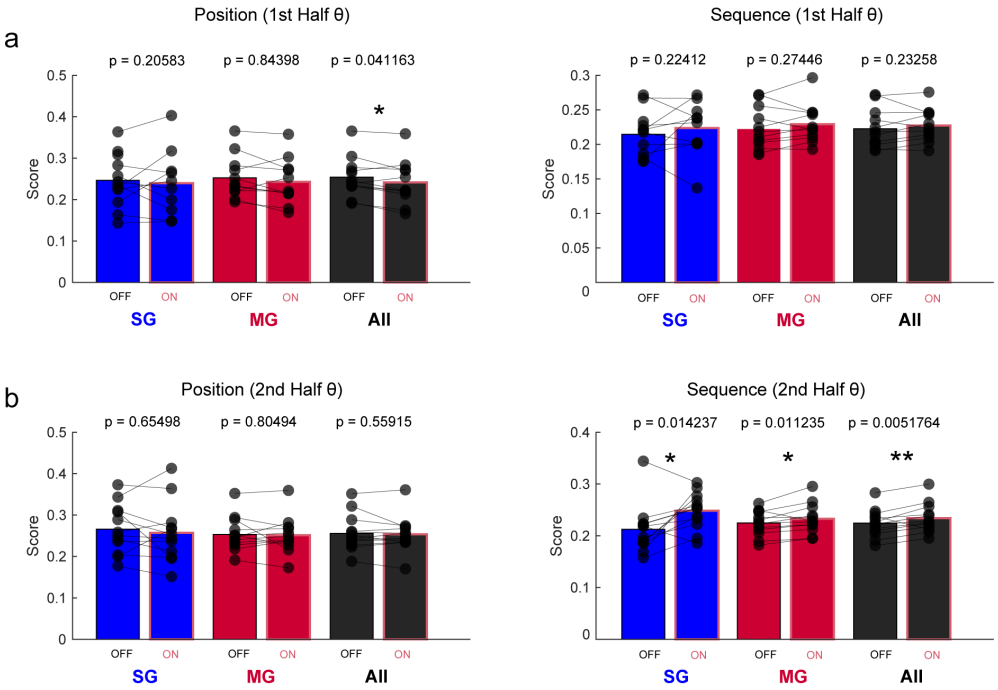

Fig. S7 Bayesian decoding across the theta cycle. (a) Comparison of mean positional and sequential scores between laser OFF vs laser ON periods in different gamma conditions (slow gamma in blue, medium gamma in red, all periods in black) in the first half of the theta cycle. Paired t test. Statistical values in order of appearance, * = p<0.05. Position: p = 0.20583, p = 0.84398, p = 0.041163. Sequence: p = 0.22412, p = 0.27446, p = 0.23258. (b) Comparison of mean positional and sequential scores between different gamma conditions (slow gamma in blue, medium gamma in red, all periods in black) in the second half of the theta cycle. Paired t test. Statistical values in order of appearance; ** = p<0.01, * = p<0.05. Position: p = 0.65498, p = 0.80494, p = 0.55915. Sequence: p = 0.014237, p = 0.011235, p = 0.0051764.

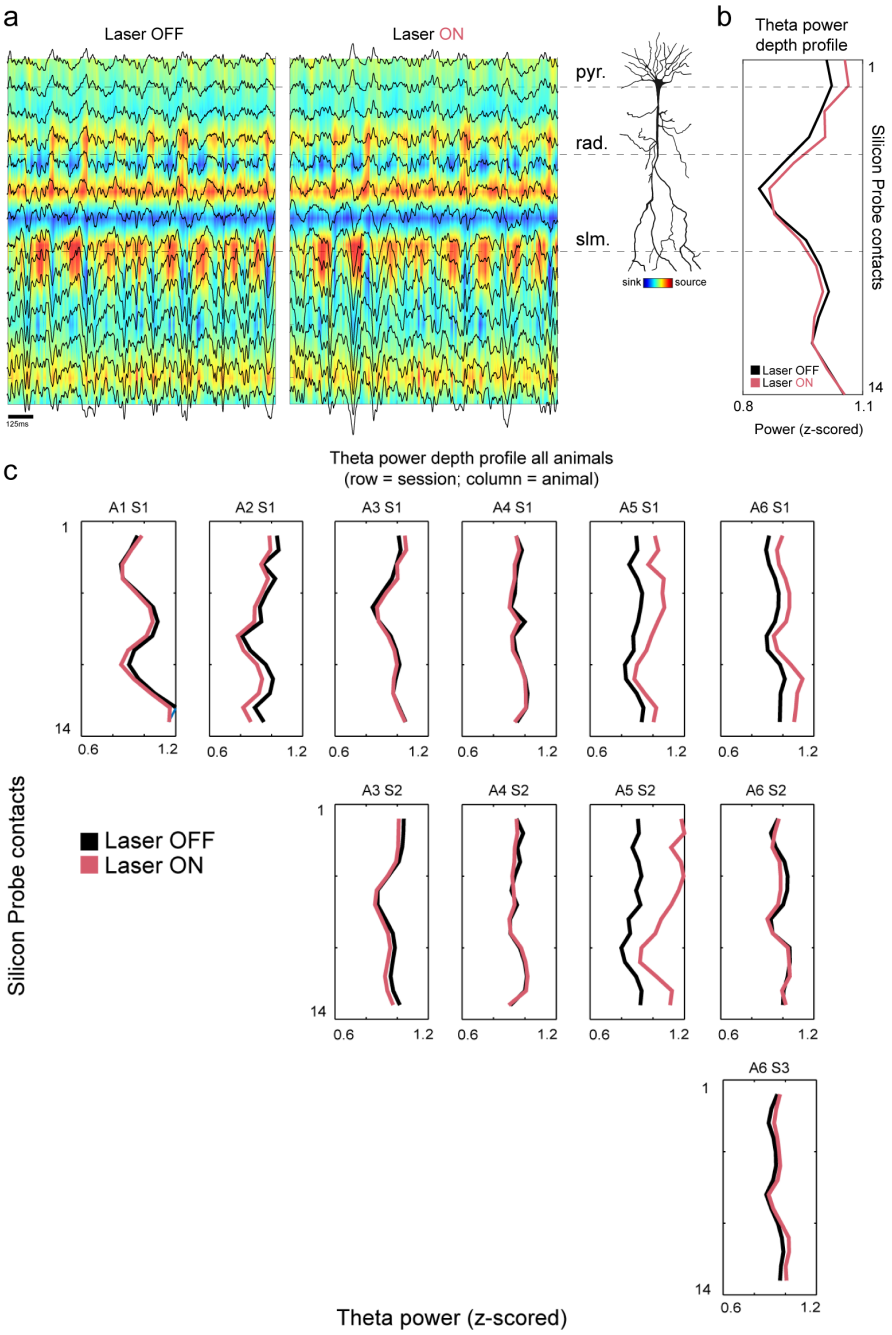

Fig. S8 Layer-resolved theta power profiles (6-10 Hz) in CA1 during optogenetic inhibition of EC LIII direct input. (a) Representative examples of color coded sink and sources currents during Laser OFF and Laser ON periods. Local field potential traces are superimposed in black. Silicon probe contacts span all CA1 layers. (b) Average theta power depth profile, same session as in (a). (c) Theta power profiles across CA1 layers. All animals (N=6), all session (n=11). No differences are found between conditions (Laser OFF vs Laser ON) - especially in the s.l.m., where EC LIII connections reach CA1 pyramidal neurons. Higher power profiles in both sessions of the Animal 5 are due to statistically different velocity performances during Laser OFF and Laser ON runs (Figure S2) - faster velocities coincide with higher power in hippocampal oscillations at all frequency bands [1].

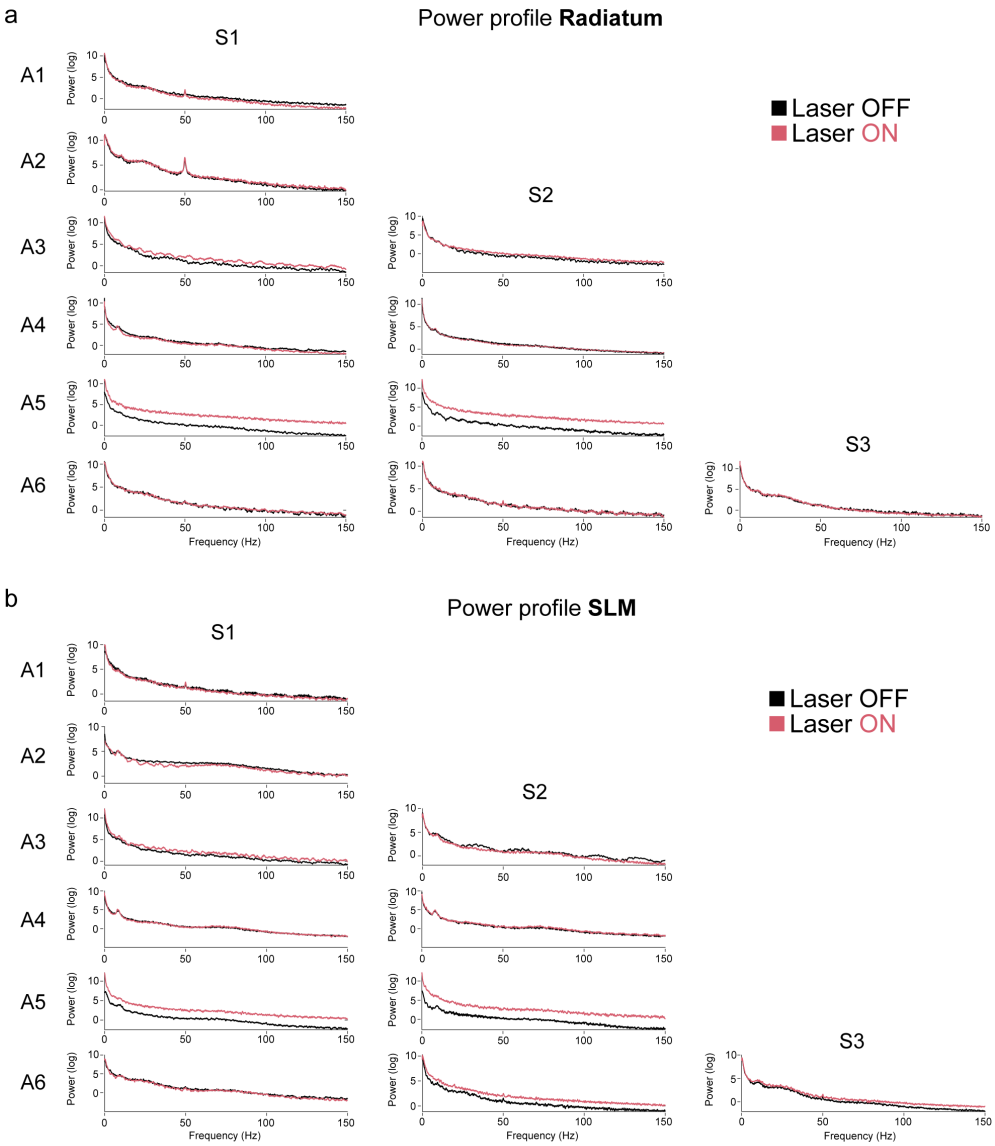

Fig. S9 Layer-resolved power spectral density estimate in CA1 during optogenetic inhibition of EC LIII direct input. (a-b)Power spectral density estimate of CSD signals in s.r. (a) and s.l.m. (b). All animals (N=6), all session (n=11), all velocities. No differences are found between conditions (Laser OFF vs Laser ON). Higher power profiles in both sessions of the Animal 5 are due to statistically different velocity performances during laser OFF and Laser ON runs (Figure S2) - faster velocities coincide with higher power in hippocampal oscillations at all frequency bands [1].

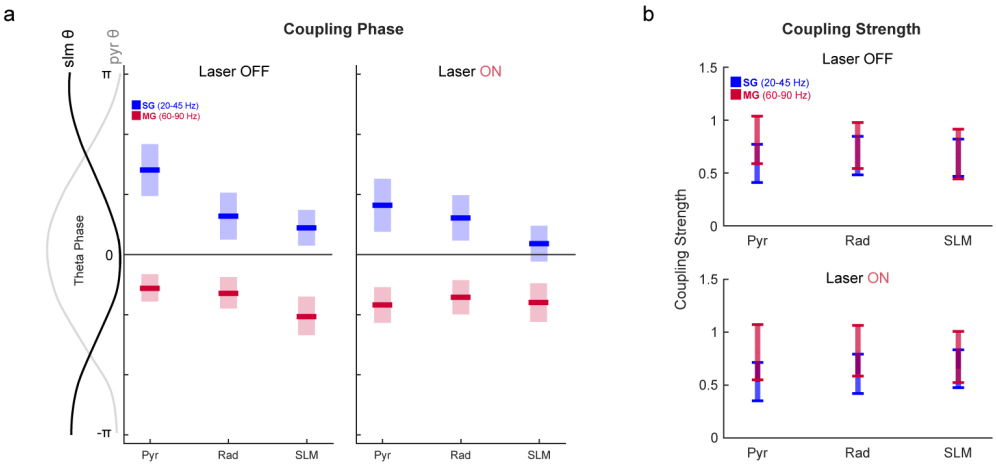

Fig. S10 Theta-gamma coupling properties in CA1 during transient optogenetic inhibition of EC LIII direct input. (a) Theta phase preference profiles of the slow and medium gamma components across CA1 layers. SG = slow gamma (20-45 Hz). MG = medium gamma (60-90 Hz). (b) Coupling strength profiles of the slow and medium gamma components across CA1 layers.

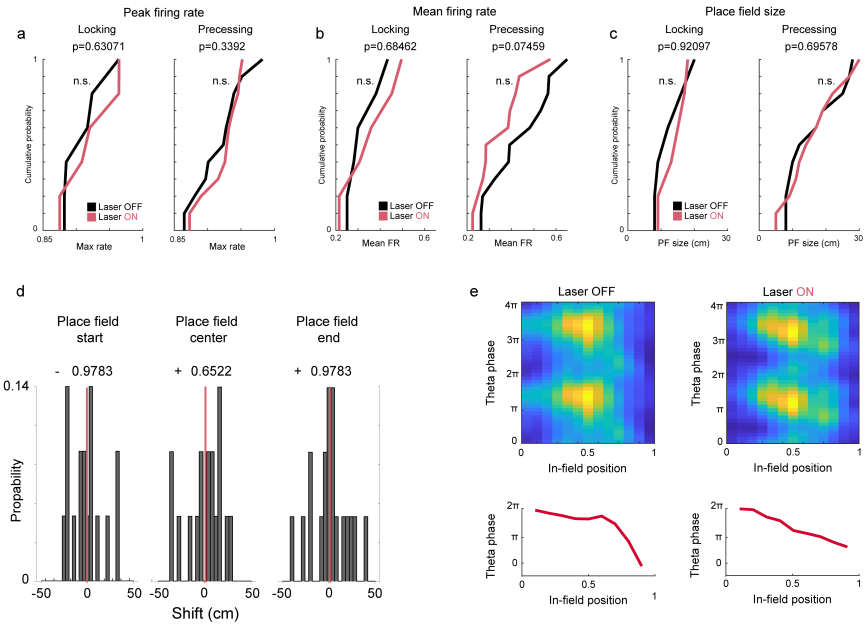

Fig. S11 Rate and phase code dynamics in a single positive control animal. (a-c) Distributions of normalized peak firing rate, mean firing rate and place field size in Laser OFF and Laser ON conditions. Animal: N=1, sessions: n=3. All comparison are not statistically significant (p>0.05; Kolmogorov–Smirnov test for all conditions, all comparison). (d)Amount of shift (in cm) on the linear track between Laser OFF and Laser ON conditions, for the place field start, place field center and place field end (mean shift start = -0.9783 cm; mean shift center= + 0.6522; mean shift end = +0.9783cm). (e) Top row, global average of the in-field spike probability during medium gamma network states, in Laser OFF (left panel) and Laser ON (right panel) runs. Bottom row, regression slope of the in-field spike probability as a function of theta phase.